OPTICA

InGaP quantum nanophotonic integrated circuits with 1.5% nonlinearity-to-loss ratio

MENGDI ZHAO[1,2,3] AND KEJIE FANG[1,3,4,*]

[1]Holonyak Micro and Nanotechnology Laboratory, University of Illinois at Urbana-Champaign, Urbana, Illinoi 61801, USA
[2]Department of Physics, University of Illinois at Urbana-Champaign, Urbana, Illinois 61801, USA
[3]Illinois Quantum Information Science and Technology Center, University of Illinois at Urbana-Champaign, Urbana, Illinois 61801, USA
[4]Department of Electrical and Computer Engineering, University of Illinois at Urbana-Champaign, Urbana, Illinois 61801, USA
*Corresponding author: kfang3@illinois.edu

Received 11 August 2021; revised 15 January 2022; accepted 24 January 2022 (Doc. ID 440383); published 18 February 2022

Optical nonlinearity plays a pivotal role in quantum information processing using photons, from heralded single-photon sources and coherent wavelength conversion to long-sought quantum repeaters. Despite the availability of strong dipole coupling to quantum emitters, achieving strong bulk optical nonlinearity is highly desirable. Here, we realize quantum nanophotonic integrated circuits in thin-film InGaP with, to our knowledge, a record-high ratio of 1.5% between the single-photon nonlinear coupling rate ($g/2\pi = 11.2$ MHz) and cavity-photon loss rate. We demonstrate second-harmonic generation with an efficiency of $71200 \pm 10300\%/\mathrm{W}$ in the InGaP photonic circuit and photon-pair generation via degenerate spontaneous parametric downconversion with an ultrahigh rate exceeding 27.5 MHz/μW—an order of magnitude improvement of the state of the art—and a large coincidence-to-accidental ratio up to 1.4×10^4. Our work shows InGaP as a potentially transcending platform for quantum nonlinear optics and quantum information applications.

https://doi.org/10.1364/OPTICA.440383

1. INTRODUCTION

Optical nonlinearity is indispensable for a number of quantum information protocols using photons. A figure of merit characterizing nonlinear quantum systems is the ratio of single-photon nonlinear coupling rate (g) and photon loss rate (κ), which roughly measures how fast quantum information can be manipulated before it is lost. Deterministic quantum logic gates can be realized in the strong coupling regime (i.e., $g/\kappa > 1$), for example, via cavity–quantum electrodynamics systems. Surprisingly, weak optical nonlinearity marked by $g/\kappa < 1$, which is typical for systems with bulk nonlinear susceptibilities, might enable alternative protocols for quantum communication and computation, besides its wide use for (heralded) single-photon generation. For example, when accompanied with ancillary coherent states, weak optical nonlinearity might enable quantum non-demolition measurement of flying photons, which is useful for relaying quantum information [1–3]. Moreover, continuous-variable cluster states synthesized from the squeezed vacuum have been proposed to implement fault-tolerant quantum computing when the squeezing exceeds certain thresholds [4–6]. These protocols, while avoiding the strong coupling regime, nevertheless might still need a nonlinearity-to-loss ratio g/κ beyond those typically achievable with bulk nonlinear optical structures.

One method to enhance photon–photon interaction via bulk nonlinear susceptibilities is to make optical micro-cavities and circuits such that the photons confined in wavelength-scale structures interact accumulatively throughout their lifetimes. The key to this approach is a thin-film material platform that yields, simultaneously, a large nonlinear mode coupling and low optical losses, thus large g/κ. In particular, photonic integrated circuits have been developed in a growing number of thin-film materials with substantial second-order nonlinear susceptibility ($\chi^{(2)}$), such as gallium arsenide (GaAs) [7,8] and aluminum GaAs [9,10]. However, these III-V materials are associated with intrinsic optical losses due to, for example, two-photon or sub-bandgap absorption at near-infrared and telecom wavelengths [11]. Recently, wide bandgap materials, including aluminum nitride [12,13] and lithium niobate [14–17], are emerging among the leading nonlinear photonic platforms. With microcavities of ultrahigh quality factors realized, these material systems have yielded second-harmonic generation (SHG) with an unprecedented efficiency [16] and ultra-bright heralded single-photon sources [17].

Here, we explore another III-V material, indium gallium phosphide (InGaP), and demonstrate its unique strength for quantum nonlinear optics and quantum information applications. InGaP has a large second-order nonlinear susceptibility ($\chi^{(2)} \approx 220$ pm/V [18]) comparable to GaAs and a sizable bandgap of about 1.9 eV that helps suppress two-photon absorption at telecom wavelengths. Previous studies of InGaP nonlinear photonics focused on using its Kerr nonlinearity in waveguides and photonic crystal cavities for frequency combs and optical parametric oscillators [19,20]. We explore its substantial second-order nonlinearity and develop an insulator-on-top fabrication

process to realize high-Q quasi-phase-matched microring resonators with strongly coupled 1550 nm and 775 nm wavelength modes in thin-film InGaP. We observed a nonlinear coupling rate of $g/2\pi = 11.2$ MHz and a nonlinearity-to-loss ratio $g/\kappa = 1.5\%$ in InGaP microring resonators, both of which are the highest among all demonstrated nonlinear photonic platforms [7,13,16,17,21]. Further, we show photon-pair generation via degenerate spontaneous parametric downconversion (SPDC) with an ultrahigh rate exceeding 27.5 MHz/μW, which is an order of magnitude higher than the previously reported record in periodically poled lithium niobate microrings [17], and a large coincidence-to-accidental ratio (CAR) up to 1.4×10^4.

2. DEVICE DESIGN AND SIMULATION

The devices deployed in this study are waveguide-coupled doubly-resonant microring resonators. The microring resonator supports fundamental 1550 nm and second-harmonic 775 nm resonances coupled via second-order optical nonlinearity. The interaction between the two resonances can be described by the Hamiltonian $\hat{H} = \hbar(g\hat{a}^{\dagger 2}\hat{b} + g^*\hat{a}^2\hat{b}^\dagger)$, where $\hat{a}(\hat{a}^\dagger)$ and $\hat{b}(\hat{b}^\dagger)$ are the annihilation (creation) operators for the fundamental and second-harmonic resonance, respectively, and g is the single-photon mode coupling coefficient. For the disordered InGaP used in this study with a zinc blende crystal structure, its second-order nonlinear optical susceptibility has only the component $\chi^{(2)}_{xyz}$, leading to a mode coupling coefficient given by [22]

$$g = \sqrt{\frac{\hbar\omega_a^2\omega_b}{8\epsilon_0}} \frac{\int d\mathbf{r}\chi^{(2)}_{xyz} \sum_{i\neq j\neq k} E^*_{ai}E^*_{aj}E_{bk}}{\int d\mathbf{r}\varepsilon_{ra}|\mathbf{E}_a|^2\sqrt{\int d\mathbf{r}\epsilon_{rb}|\mathbf{E}_b|^2}}, \quad (1)$$

where $\omega_{a(b)}$ is the angular frequency of resonance a (b), $\mathbf{E}_{a(b)}$ is the modal electric field, ϵ_0 is the vacuum permittivity, and is the relative permittivity at 1550 nm (775 nm). The z direction is defined to be perpendicular to the device plane.

To optimize g, and thus the device-level nonlinearity, modes a and b need to be phase-matched and have a substantial field overlap defined by the inter-modal integral in Eq. (1). We choose the fundamental transverse-electric mode (TE_{00}) and fundamental transverse-magnetic mode (TM_{00}) for the 1550 nm and 775 nm resonances [Fig. 1(a)], respectively, taking advantage of their dominant in-plane (for TE_{00}) and out-of-plane (for TM_{00}) electric field components. The $\chi^{(2)}_{xyz}$ nonlinear susceptibility imposes the energy conservation and quasi-phase-matching condition [23] between the two traveling-wave resonances for maximal coupling (Supplement 1), i.e.,

$$2\omega_a = \omega_b, \quad |2m_a - m_b| = 2, \quad (2)$$

where $m_{a(b)}$ is the azimuthal number of resonance $a(b)$.

Because of the strong dispersion of InGaP with a refractive index of $n = 3.12$ at 1550 nm and $n = 3.41$ at 775 nm [24], the quasi-phase-matching condition can be satisfied only in thin InGaP microrings with high-aspect-ratio cross sections. Figure 1(b) shows the dispersion of the TE_{00} mode with $m_a = 36$ and TM_{00} modes with $m_b = 2m_a \pm 2$ for the 115 nm thick microring with a center radius of $R = 5$ μm. The crossing points of the dispersion curves thus yield the ring width, around 945 nm and 1360 nm, respectively, satisfying Eq. (2). A thin layer (50 nm) of silicon dioxide on top of the suspended InGaP microring is included in the simulated structure, in accordance with the fabricated device (see Section 3). Using $\chi^{(2)}_{xyz} = 220$ pm/V [18], we numerically find a coupling coefficient $g/2\pi = 10.90(5.96)$ MHz between the 1550 nm TE_{00} and 775 nm TM_{00} resonances of the 5 μm microring satisfying the quasi-phase-matching condition $m_b = 2m_a + 2(m_b = 2m_a - 2)$. It is worth noting that g scales approximately as $R^{-0.5}$, and thus smaller microring resonators will yield a larger nonlinear coupling, though photon lifetimes might be sacrificed due to excess scattering and bending losses. Figure 1(c) reveals that the quasi-phase-matching condition is sensitive to the thickness of InGaP films, requiring uniform InGaP films for optimized devices.

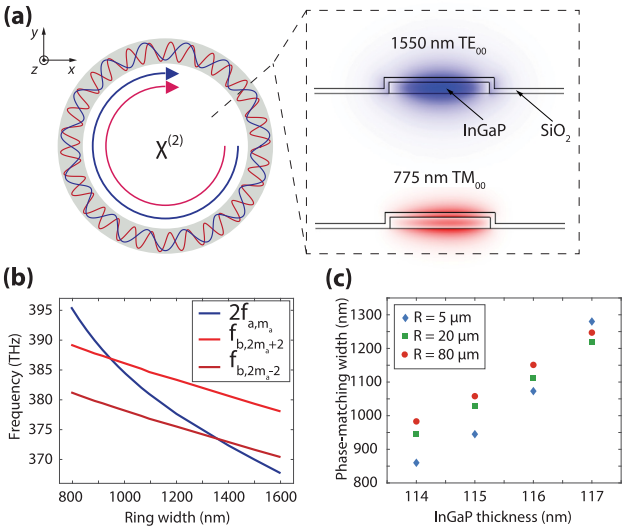

Fig. 1. (a) Schematic plot of a $\chi^{(2)}$ microring resonator. Inset shows the electric field of the 1550 nm TE_{00} resonance (E_r component) and 775 nm TM_{00} resonance (E_z component) at the cross section of the microring. (b) Dispersion curve of the fundamental mode with azimuthal number $m_a = 36$ and second-harmonic modes with azimuthal number $m_b = 2m_a \pm 2$. The microring has a thickness of 115 nm and $R = 5$ μm. (c) Width of the microring satisfying the phase-matching condition $m_b = 2m_a + 2$ between the 1550 nm and 775 nm resonances.

3. DEVICE FABRICATION

The devices are fabricated from 115 nm thick (measured by scanning electron microscopy) disordered InGaP films grown on GaAs substrate (2 deg off-cut toward [110]) by metal–organic chemical vapor deposition (T = 545 C, V/III = 48, precursors: trimethylindium, trimethylgallium, and PH_3). The photoluminescence and x-ray measurements reveal a composition of disordered $In_{0.48}Ga_{0.52}P$ with a 1.92 eV bandgap. The root-mean-square surface roughness of the InGaP thin film is about 0.32 nm measured by atomic-force microscopy (AFM) [Fig. 2(a)]. The device pattern is defined using 150 keV electron beam lithography and 150 nm negative tone resist hydrogensilsesquioxane (HSQ). A 20 nm thick layer of silicon dioxide is deposited on InGaP via plasma-enhanced chemical vapor deposition (PECVD) to enhance the adhesion of HSQ. The pattern is transferred to InGaP via inductively coupled plasma reactive-ion etch (ICP-RIE) using $Cl_2/CH_4/Ar$ gas mixture with a selectivity of InGaP: HSQ: PECVD $SiO_2 = 240:90:80$. After a short buffered oxide etch to remove the residual oxide (both HSQ and PECVD oxide), a layer of 50 nm thick silicon dioxide is deposited on the chip via

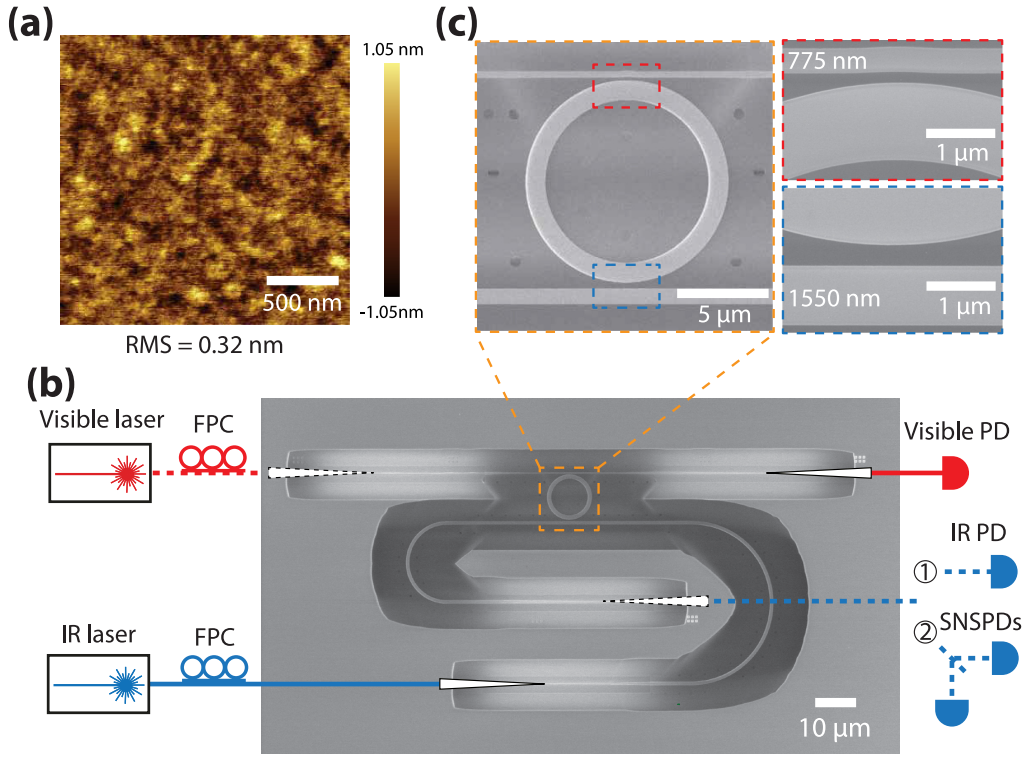

Fig. 2. (a) Surface morphology of the 115 nm thick InGaP-on-GaAs film in a 2 μm × 2 μm region measured by AFM. The root mean square (RMS) of the surface roughness is 0.32 nm. (b), (c) Scanning electron microscopy images of the fabricated device and schematic of the measurement setup. Second-harmonic generation and photon-pair generation are measured via solid and dashed paths, respectively. IR, infrared; FPC, fiber polarization controller; PD, photodetector; SNSPD, superconducting nanowire single-photon detector.

atomic layer deposition. A second electron beam lithography and subsequent ICP-RIE using CHF_3 gas are applied to pattern etch-through holes in the silicon dioxide layer for undercut of the InGaP device. Finally, the InGaP device is released from the GaAs substrate using citric-acid-based selective etching [25]. The suspended InGaP device is mechanically anchored to the silicon dioxide membrane (see Supplement 1 for additional information and a schematic of the fabrication process).

Figures 2(b) and 2(c) show scanning electron microscopy images of the fabricated device. The microring resonator is coupled to two bus waveguides for transmitting the 1550 nm and 775 nm wavelength light. The 1550 nm wavelength straight waveguide is 800 nm wide and separated from the ring by 400 nm. It decouples from the 775 nm TM_{00} microring resonance because of the tight field confinement of the latter and the large ring-waveguide gap. On the other hand, the 775 nm wavelength pulley waveguide is 280 nm wide with a wrap angle of 6 deg and a ring-waveguide gap of 250 nm. It decouples from the 1550 nm TE_{00} microring resonance because of the significantly different mode index of the 1550 nm TE_{00} mode in the narrow waveguide and the wide microring. In this way, we are able to separately transmit 1550 nm and 775 nm wavelength light in the two waveguides without cross talk and independently control the external quality factors of the 1550 nm and 775 nm microring resonances. The bus waveguides are connected to adiabatically tapered couplers for transmitting TE- or TM-polarized light between the photonic integrated circuits and single-mode optical fibers (Supplement 1).

4. DEVICE CHARACTERIZATION

The transmission spectrum of the microring resonator is measured using two tapered fibers evanescently coupled to the waveguide couplers. The measured coupling efficiency is about 60% and 33% for the 1550 nm TE-polarized and 775 nm TM-polarized light, respectively (Supplement 1). Figure 3(a) shows the transmission spectrum of a 5 μm radius microring, where the 1550 nm band TE_{00} and 775 nm band $TM_{00,10,20,30}$ resonances are observed and identified by their free spectral ranges. The quality factor of the resonance is obtained by fitting the transmission spectrum using the input–output formula (Supplement 1). We also measured the quality factor of the 1550 nm band TE_{00} resonance of 20 μm and 80 μm radius microrings, which is shown in Fig. 3(b). The similarity of the intrinsic quality factor of microrings of different sizes indicates that the dominant optical loss is likely due to the surface roughness of InGaP films and/or etched sidewalls instead of waveguide bending for the ring radius down to 5 μm. The quality factor is probably not limited by material absorption because both wavelengths (1550 nm and 775 nm) are below the bandgap of InGaP, and we do not observe power-dependent loss for the power the device is operated at due to nonlinear absorption, such as two-photon absorption. However, we abstain from making smaller resonators because the gain of mode coupling will be marginal, while the waveguide bending loss and the scattering loss due to sidewall roughness might become excessive.

The nonlinear mode coupling is characterized via SHG in quasi-phase-matched 5 μm radius microring resonators. By sweeping the pump laser wavelength across the 1550 nm band in a group of devices with varying ring widths and measuring the

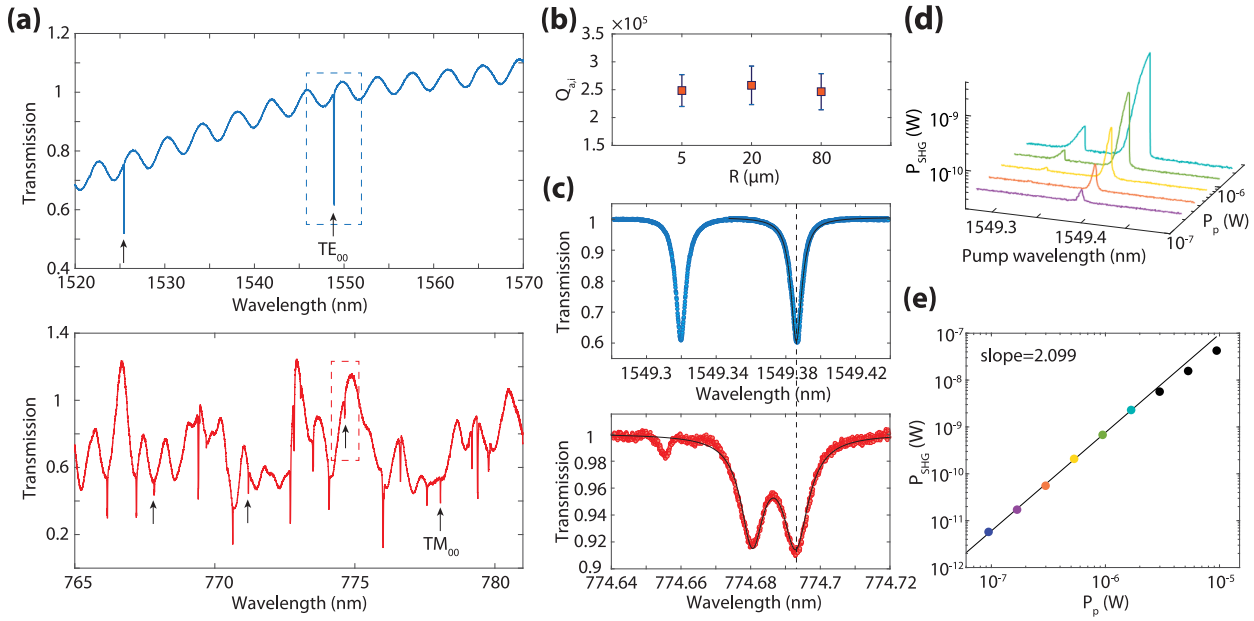

Fig. 3. (a) Transmission spectrum of a 5 μm radius microring in the 1550 nm TE and 775 nm TM bands. (b) Intrinsic quality factor of 1550 nm TE_{00} resonances of microrings with different radii. The error bar represents the standard deviation of the quality factor. Eight resonances are measured for each size of the ring resonator. (c) Normalized transmission spectrum of a pair of phase-matched fundamental and second-harmonic resonances (highlighted by the dashed line), corresponding to the boxed resonances in (a). (d) SHG signal for various pump powers (color-coded with the corresponding peak powers given in (e). (e) Peak SHG power (subtracted with the background) versus pump power. The line fitted to the colored data points illustrates the quadratic relationship between the SHG and pump power.

SHG signal power, we are able to identify quasi-phase-matched rings and resonances thereof. Finally, the slight frequency mismatch between the fundamental and second-harmonic resonances could be eliminated by temperature tuning, utilizing their different thermo-optic responses, which are roughly 40 pm/K and 17 pm/K for the 1550 nm TE_{00} and 775 nm TM_{00} resonances, respectively. The measured ring width of the quasi-phase-matched device is about 1130 nm. The discrepancy from the simulation result (945 nm) might be due to the difference of refractive index of the actual InGaP film from the value used in the simulation or the imprecision of InGaP thickness measurement [see Fig. 1(c)]. Figure 3(c) shows the spectra of a pair of frequency-matched 1550 nm and 775 nm resonances satisfying the frequency- and phase-matching conditions. Due to the surface-roughness-induced backscattering, these are standing-wave resonances resulted from the hybridization of the degenerate clockwise and counterclockwise traveling-wave resonances. Using this pair of frequency-matched resonances, we measured the SHG signal with a continuous-wave pump for various powers [Figs. 3(d) and 3(e)]. The side peak in Fig. 3(d) is from the other split fundamental resonance that is frequency-detuned from the same second-harmonic resonance. The deviation from the quadratic relationship for more intense pumps is due to thermo-optic shift of the resonances instead of pump depletion as seen from Fig. 3(d). However, power handling of the released device can be improved with thicker oxide cladding for better thermal conduction. The on-chip SHG efficiency is 71200 ± 10300%/W after normalizing out the fiber-optic coupler efficiency (Supplement 1), where the error is the standard deviation of the measured SHG efficiency among different pump powers. We note that the SHG efficiency of our device is significantly higher than a recent demonstration in thick InGaP waveguides [26]. Together with the measured intrinsic and external quality factors of the two resonances, i.e., $Q_{a(b),i} \equiv \omega_{a(b)}/\kappa_{a(b),i} = 2.63 \times 10^5 (9.58 \times 10^4)$ and $Q_{a(b),e} \equiv \omega_{a(b)}/\kappa_{a(b),e} = 9.12 \times 10^5 (2.12 \times 10^6)$, where $\kappa_{a(b),e}$ and $\kappa_{a(b),i}$ are the external and intrinsic photon (energy) loss rate of the resonances, respectively, we extract the mode coupling coefficient $g/2\pi = 11.18 \pm 0.81$ MHz (Supplement 1), which is close to the theoretical value for the device satisfying $m_b = 2m_a + 2$.

We use a figure of merit, $g/\kappa_{a,i}$, to benchmark the strength of optical nonlinearity relative to the intrinsic photon loss of the doubly-resonant $\chi^{(2)}$ cavity. The InGaP microring resonator of this work yields $g/\kappa_{a,i} = 1.52 \pm 0.11\%$, which is the highest

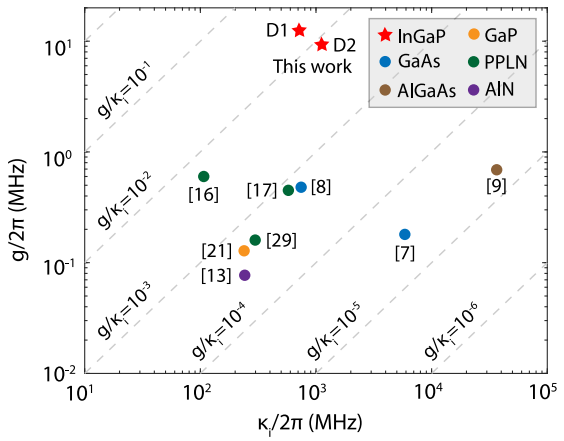

Fig. 4. Nonlinear mode coupling coefficient (g) and intrinsic photon loss rate of the fundamental mode (κ_i) of microring resonators made from various $\chi^{(2)}$ materials, including InGaP (this work; D1 and D2 are the devices used for SHG and SPDC experiments, respectively), GaAs (238 pm/V [27]) [7,8], $Al_xGa_{1-x}As$ (<238 pm/V decreasing with x [28]) [9], GaP (70 pm/V [27]) [21], periodically poled lithium niobate (PPLN) (54 pm/V) [16,17,29], and AlN (1–6 pm/V) [13]. The value of the dominant $\chi^{(2)}$ component of each material at 1.5 μm is indicated in parentheses.

Table 1. Scaling of the Figure of Merit of Some $\chi^{(2)}$ Nonlinear Processes[a]

$\chi^{(2)}$ Nonlinear Process	Scaling
SHG efficiency	$g^2/\kappa_a^2\kappa_b$ [30]
SPDC photon-pair rate	$g^2/\kappa_a\kappa_b$ [12]
OPO pump threshold	$\kappa_a^2\kappa_b/g^2$ [31]
Squeezed light pump	$\kappa_a^2\kappa_b/g^2$ [31]
Two-photon transport amplitude	$g^2/\kappa_a\kappa_b$ [32,33]

[a]OPO, optical parametric oscillation. Pump for squeezed light is assumed for optimal quadrature noise squeezing (i.e., $\kappa_{a,i}/\kappa_a$). Two-photon transport is the process of two a-mode photons interacting via a waveguide-coupled $\chi^{(2)}$ cavity without any parametric pump, in contrast to the other four nonlinear processes.

among all demonstrated nonlinear photonic platforms (see Fig. 4). We also calculated $g^2/(\kappa_{a,i}\kappa_{b,i})$. For the InGaP SHG device, it is 4.2×10^{-5}. In comparison, the $LiNbO_3$ device in [16] yields 1.9×10^{-5}. We choose κ_i instead of the total loss rate in calculating the figure of merit because κ_e might be chosen differently depending on the specific application without altering κ_i substantially. A majority of nonlinear optical processes, especially those relevant to quantum information applications, possess figures of merit that scale with $(g/\kappa)^2$ (Table 1). For example, the quantum non-demolition measurement of photons [1,3] relies on the two-photon transport amplitude via a $\chi^{(2)}$ medium, which is proportional to $(g/\kappa)^2$ [32,33]. The InGaP nonlinear photonic platform is expected to significantly enhance these nonlinear optical processes for quantum information applications.

5. PHOTON-PAIR GENERATION

Here, we utilize the InGaP microring resonator with a sizable g/κ to demonstrate highly efficient photon-pair generation via degenerate SPDC. For this purpose, we use a 5 μm radius microring that is near critical coupling to both 775 nm and 1550 nm light waveguides, which is achieved by adjusting the ring-waveguide gap and waveguide wrap angle. The quality factors of a pair of phase- and frequency-matched resonances are $Q_{a(b),i} = 1.75 \times 10^5 (6.18 \times 10^4)$ and $Q_{a(b),e} = 2.77 \times 10^5 (1.13 \times 10^5)$, respectively. We pump the 775 nm resonance and characterize the SPDC photons from the 1550 nm resonance using two superconducting nanowire single-photon detectors (SNSPDs) (Quantum Opus, 85% efficiency, 100 Hz dark count rate) in the Hanbury Brown–Twiss setup [Fig. 2(b)]. The SPDC signal is passed through two wavelength-division filters, each with a 40 dB extinction ratio, for filtering out the leak-through pump photons before sending to SNSPDs. The measured second-order correlation function of the SPDC photon pair shows a clear bunching effect [Fig. 5(a)]. The pair-generation rate (PGR) and CAR corresponding to various pump powers are shown in Fig. 5(b) (see Supplement 1 for detailed analysis). Here, CAR is measured as $C/A - 1$, where C is the coincident counts at the coincidence peak, and A is the accidental counts estimated by averaging the background counts away from the peak. The coincidence window is chosen to be 50 ps, which is close to $1/\kappa_a = 87$ ps. Because the device is operated in the weak driving limit, i.e., $g\sqrt{n_p} \ll \kappa_a$, where n_p is the cavity pump-photon number, the PGR scales linearly with the pump power with a per-power rate of 27.5 MHz/μW, which is close to the theoretical value of 41.8 MHz/μW. The discrepancy is possibly due to the slight frequency mismatch of the two resonances and pump detuning. From the photon-PGR, we are able to obtain $g/\kappa_{a,i} = 0.81\%$ for this device. The InGaP photon-pair source also shows an excellent CAR up to 1.4×10^4. Compared to other cavity-based SPDC photon-pair sources [Fig. 5(c)], the photon-pair generation efficiency, i.e., PGR at 1 μW pump power, of our InGaP microring resonator is an order of magnitude larger than the best reported value in integrated photonic platforms [17], while the noise figure is on par with typical $\chi^{(2)}$ sources. The photon-pair spectral efficiency, i.e., the per-power per-bandwidth rate, of the InGaP device is 1.5×10^4 W^{-1} compared to 1.4×10^3 W^{-1} of [17]. Note that in principle, CAR inversely scales with PGR, and CAR of degenerate SPDC is half that of non-degenerate SPDC, which explains the factor of two difference between the CAR of our device and that of Refs. [17,37].

6. DISCUSSION

In summary, we have developed quantum nanophotonic integrated circuits in InGaP thin films with a record-breaking nonlinearity-to-loss ratio, leading to an order-of-magnitude enhancement of photon-PGR compared to other nonlinear photonic platforms. The InGaP platform is expected to enhance and enable other nonlinear optical effects on chips and even observation of single-photon interactions. The oxide-on-top, suspended device architecture allows us to fabricate integrated photonic circuits in index-matched material systems without complicated wafer bonding and transfer. We point out that the suspended device architecture is not fundamentally limited in terms of power handling, which can be enhanced by increasing the thickness of the oxide top cladding. It is promising to further improve the nonlinearity-to-loss ratio of the InGaP platform by reducing the roughness-induced photon scattering loss through, for example,

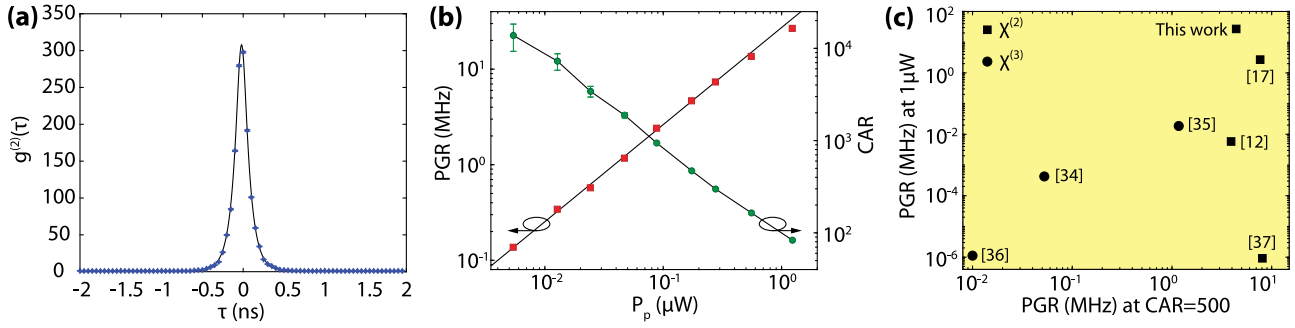

Fig. 5. (a) Second-order correlation function of the SPDC photons for 0.28 μW on-chip pump power. (b) PGR and CAR versus pump power. The straight line is the linear fit to the PGR data with a slope of 27.5 MHz/μW. Error bar is estimated using shot noise. (c) Comparison of SPDC photon-pair sources [12,17,34–37] in terms of PGR for 1 μW pump power (i.e., efficiency) and PGR with CAR = 500 (i.e., noise figure).

tuning the III-V material growth condition [38] and optimizing the etching process. Further, the InGaP platform is uniquely positioned, with the possibility to integrate with other III-V materials [39,40], for realizing quantum photonic microchips with integrated lasers, photodetectors, and linear and nonlinear device components.

Funding. National Science Foundation (DMS 18-39177).

Disclosures. The authors declare no conflicts of interest.

Data availability. Data underlying the results presented in this paper are available from the corresponding author upon reasonable request.

Supplemental document. See Supplement 1 for supporting content.

REFERENCES

1. K. Nemoto and W. J. Munro, "Nearly deterministic linear optical controlled-NOT gate," Phys. Rev. Lett. **93**, 250502 (2004).
2. W. J. Munro, K. Nemoto, and T. P. Spiller, "Weak nonlinearities: a new route to optical quantum computation," New J. Phys. **7**, 137 (2005).
3. K. Xia, M. Johnsson, P. L. Knight, and J. Twamley, "Cavity-free scheme for nondestructive detection of a single optical photon," Phys. Rev. Lett. **116**, 023601 (2016).
4. N. C. Menicucci, "Fault-tolerant measurement-based quantum computing with continuous-variable cluster states," Phys. Rev. Lett. **112**, 120504 (2014).
5. K. Fukui, A. Tomita, A. Okamoto, and K. Fujii, "High-threshold fault-tolerant quantum computation with analog quantum error correction," Phys. Rev. X **8**, 021054 (2018).
6. B. Q. Baragiola, G. Pantaleoni, R. N. Alexander, A. Karanjai, and N. C. Menicucci, "All-Gaussian universality and fault tolerance with the Gottesman-Kitaev-Preskill code," Phys. Rev. Lett. **123**, 200502 (2019).
7. P. S. Kuo, J. Bravo-Abad, and G. S. Solomon, "Second-harmonic generation using-quasi-phasematching in a GaAs whispering-gallery-mode microcavity," Nat. Commun. **5**, 3109 (2014).
8. L. Chang, A. Boes, P. Pintus, J. D. Peters, M. Kennedy, X.-W. Guo, N. Volet, S.-P. Yu, S. B. Papp, and J. E. Bowers, "Strong frequency conversion in heterogeneously integrated GaAs resonators," APL Photon. **4**, 036103 (2019).
9. S. Mariani, A. Andronico, A. Lematre, I. Favero, S. Ducci, and G. Leo, "Second-harmonic generation in AlGaAs microdisks in the telecom range," Opt. Lett. **39**, 3062–3065 (2014).
10. S. May, M. Kues, M. Clerici, and M. Sorel, "Second-harmonic generation in AlGaAs-on-insulator waveguides," Opt. Lett. **44**, 1339–1342 (2019).
11. C. Michael, K. Srinivasan, T. Johnson, O. Painter, K. Lee, K. Hennessy, H. Kim, and E. Hu, "Wavelength-and material-dependent absorption in GaAs and AlGaAs microcavities," Appl. Phys. Lett. **90**, 051108 (2007).
12. X. Guo, C.-L. Zou, C. Schuck, H. Jung, R. Cheng, and H. X. Tang, "Parametric down-conversion photon-pair source on a nanophotonic chip," Light Sci. Appl. **6**, e16249 (2017).
13. A. W. Bruch, X. Liu, X. Guo, J. B. Surya, Z. Gong, L. Zhang, J. Wang, J. Yan, and H. X. Tang, "17 000%/W second-harmonic conversion efficiency in single-crystalline aluminum nitride microresonators," Appl. Phys. Lett. **113**, 131102 (2018).
14. R. Luo, Y. He, H. Liang, M. Li, and Q. Lin, "Highly tunable efficient second-harmonic generation in a lithium niobate nanophotonic waveguide," Optica **5**, 1006–1011 (2018).
15. M. Zhang, B. Buscaino, C. Wang, A. Shams-Ansari, C. Reimer, R. Zhu, J. M. Kahn, and M. Lončar, "Broadband electro-optic frequency comb generation in a lithium niobate microring resonator," Nature **568**, 373–377 (2019).
16. J. Lu, M. Li, C.-L. Zou, A. Al Sayem, and H. X. Tang, "Toward 1% single-photon anharmonicity with periodically poled lithium niobate microring resonators," Optica **7**, 1654–1659 (2020).
17. Z. Ma, J.-Y. Chen, Z. Li, C. Tang, Y. M. Sua, H. Fan, and Y.-P. Huang, "Ultrabright quantum photon sources on chip," Phys. Rev. Lett. **125**, 263602 (2020).
18. Y. Ueno, V. Ricci, and G. I. Stegeman, "Second-order susceptibility of $Ga_{0.5}In_{0.5}P$ crystals at 1.5 μm and their feasibility for waveguide quasi-phase matching," J. Opt. Soc. Am. B **14**, 1428–1436 (1997).
19. U. D. Dave, C. Ciret, S.-P. Gorza, S. Combrie, A. De Rossi, F. Raineri, G. Roelkens, and B. Kuyken, "Dispersive-wave-based octave-spanning supercontinuum generation in InGaP membrane waveguides on a silicon substrate," Opt. Lett. **40**, 3584–3587 (2015).
20. G. Marty, S. Combrié, F. Raineri, and A. De Rossi, "Photonic crystal optical parametric oscillator," Nat. Photonics **15**, 53–58 (2021).
21. A. D. Logan, M. Gould, E. R. Schmidgall, K. Hestroffer, Z. Lin, W. Jin, A. Majumdar, F. Hatami, A. W. Rodriguez, and K.-M. C. Fu, "400%/W second harmonic conversion efficiency in 14 μm-diameter gallium phosphide-on-oxide resonators," Opt. Express **26**, 33687–33699 (2018).
22. R. Luo, Y. He, H. Liang, M. Li, J. Ling, and Q. Lin, "Optical parametric generation in a lithium niobate microring with modal phase matching," Phys. Rev. Appl. **11**, 034026 (2019).
23. Z. Yang, P. Chak, A. D. Bristow, H. M. van Driel, R. Iyer, J. S. Aitchison, A. L. Smirl, and J. Sipe, "Enhanced second-harmonic generation in AlGaAs microring resonators," Opt. Lett. **32**, 826–828 (2007).
24. H. Tanaka, Y. Kawamura, and H. Asahi, "Refractive indices of $In_{0.49}Ga_{0.51-x}Al_xP$ lattice matched to GaAs," J. Appl. Phys. **59**, 985–986 (1986).
25. H. Uchiyama, H. Ohta, T. Shiota, C. Takubo, K. Tanaka, and K. Mochizuki, "Fabrication of sub-transistor via holes for small and efficient power amplifiers using highly selective GaAs/InGaP wet etching," J. Vacuum Sci. Technol. B **24**, 664–668 (2006).
26. N. Poulvellarie, C. M. Arabi, C. Ciret, S. Combrié, A. De Rossi, M. Haelterman, F. Raineri, B. Kuyken, S.-P. Gorza, and F. Leo, "Efficient type II second harmonic generation in an indium gallium phosphide on insulator wire waveguide aligned with a crystallographic axis," Opt. Lett. **46**, 1490–1493 (2021).
27. I. Shoji, T. Kondo, A. Kitamoto, M. Shirane, and R. Ito, "Absolute scale of second-order nonlinear-optical coefficients," J. Opt. Soc. Am. B **14**, 2268–2294 (1997).
28. M. Ohashi, T. Kondo, R. Ito, S. Fukatsu, Y. Shiraki, K. Kumata, and S. Kano, "Determination of quadratic nonlinear optical coefficient of Al_xGa_{1-x} as system by the method of reflected second harmonics," J. Appl. Phys. **74**, 596–601 (1993).
29. J.-Y. Chen, Z.-H. Ma, Y. M. Sua, Z. Li, C. Tang, and Y.-P. Huang, "Ultra-efficient frequency conversion in quasi-phase-matched lithium niobate microrings," Optica **6**, 1244–1245 (2019).
30. X. Guo, C.-L. Zou, and H. X. Tang, "Second-harmonic generation in aluminum nitride microrings with 2500%/W conversion efficiency," Optica **3**, 1126–1131 (2016).
31. D. F. Walls and G. J. Milburn, *Quantum optics* (Springer, 2007).
32. S. Xu and S. Fan, "Input-output formalism for few-photon transport: a systematic treatment beyond two photons," Phys. Rev. A **91**, 043845 (2015).
33. Y. Wang and K. Fang, "Few-photon transport via a multimode nonlinear cavity: theory and applications," Phys. Rev. A **105**, 023713 (2022).
34. X. Lu, Q. Li, D. A. Westly, G. Moille, A. Singh, V. Anant, and K. Srinivasan, "Chip-integrated visible–telecom entangled photon pair source for quantum communication," Nat. Phys. **15**, 373–381 (2019).
35. C. Ma, X. Wang, V. Anant, A. D. Beyer, M. D. Shaw, and S. Mookherjea, "Silicon photonic entangled photon-pair and heralded single photon generation with CAR> 12,000 and $g^{(2)}(0)$< 0.006," Opt. Express **25**, 32995–33006 (2017).
36. X. Wang, C. Ma, R. Kumar, P. Doussiere, R. Jones, H. Rong, and S. Mookherjea, "Photon pair generation using a silicon photonic hybrid laser," APL Photon. **3**, 106104 (2018).
37. Z. Zhang, C. Yuan, S. Shen, H. Yu, R. Zhang, H. Wang, H. Li, Y. Wang, G. Deng, Z. Wang, L. You, Z. Wang, H. Song, G. Guo, and Q. Zhou, "High-performance quantum entanglement generation via cascaded second-order nonlinear processes," npj Quantum Inf. **7**, 123 (2021).
38. W. Xie, L. Chang, H. Shu, J. C. Norman, J. D. Peters, X. Wang, and J. E. Bowers, "Ultrahigh-Q AlGaAs-on-insulator microresonators for integrated nonlinear photonics," Opt. Express **28**, 32894–32906 (2020).
39. R. Phelan, M. Gleeson, D. Byrne, J. O'Carroll, P. Long, L. Maigyte, R. Lennox, K. Carney, C. Herbert, J. Somers, and B. Kelly, "InGaP/AlGaInP quantum well discrete mode laser diode emitting at 689 nm," IEEE Photon. Technol. Lett. **30**, 235–237 (2017).
40. S. Kim, H. Mohseni, M. Erdtmann, E. Michel, C. Jelen, and M. Razeghi, "Growth and characterization of InGaAs/InGaP quantum dots for midinfrared photoconductive detector," Appl. Phys. Lett. **73**, 963–965 (1998).